RESEARCH ARTICLE

NANO · MICRO small
www.small-journal.com

Pressure-Assisted Anisotropy in Carbon Nanofiber Films for Smart Electromagnetic Interference Shielding and Joule Heating

Hao Feng, Xin Zhao, Wei Qian, Zhe Wang, Pengfei Chen, Chao Tian, Bao-Wen Li,* and Daping He**

Intelligent electromagnetic interference (EMI) shielding materials with adjustable properties and performances are garnering significant attention due to the escalating complexity of application scenarios for electronic devices. Also, the trend of miniaturization is calling for lightweight and multifunctional materials. Here, the preparation of highly aligned carbon nanofiber film (a-CNFF) by electrospinning technology and a two-stage carbonization process is proposed, in which the pressurization strategy in the carbonization process promotes the development of highly aligned fiber network structures. The serialized anisotropic structures exhibit an impressive tunability in EMI shielding effectiveness (SE) adjustable from 23.0 to 35.6 dB for linearly polarized electromagnetic waves, and a superior specific SE value (SSE/t) of 34 000 dB cm^2 g^{-1}, with an EMI SE per unit thickness of 5791 dB cm^{-1}. Moreover, under a low load voltage of 1.6 V, the peak temperature of the film can be tuned within a wide range of 49.2–120.6 °C. These remarkable performances achieved by simply rotating the film demonstrate adjustable functionalities of the a-CNFF, providing guidelines in the applications of aerospace, military, microelectronics, and wearable devices.

1. Introduction

With the rapid worldwide proliferation of wireless communication that results in a surging number of wireless infrastructures,[1] we are facing an ever-rising new type of pollution called electromagnetic pollution.[2] Far beyond its effect on neighboring sensitive electronic equipment,[3] mounting evidence has shown serious biological and health effects[4] caused by unprecedented exposure to electromagnetic radiation. To date, traditional metals-based electromagnetic interference (EMI) shielding materials are still dominating the market due to their superb intrinsic electrical conductivity.[5] However, with the increasing power density and prevalence of modern electronics, these metals-based materials are finding themselves hard to adapt to the integrated devices requiring miniaturization, and portability due to large density, poor flexibility, and corrosion resistance.[6] Therefore, it is urgent to develop lightweight, flexible, and chemically stable electromagnetic shielding materials.[7] Advanced carbon materials that can be assembled into conductive macroscopic films featuring lightweight, flexible, and chemical stability, such as graphene, carbon nanotube (CNT), and carbon nanofiber (CNF) bring a new opportunity for the development of electromagnetic shielding materials.[8] Poly (m-phenylene isophthalamide) (PMIA) fiber has an abundant conjugated aromatic structure in the backbone, which is considered as a promising alternate precursor for graphitization.

In addition, the arrival of the era of intelligent electronics requires more effective electromagnetic shielding solutions to face increasingly complex application scenarios.[9] In recent years, intelligent electromagnetic interference shielding materials under different external stimuli such as temperature, humidity, stress, and pH have been realized.[10] However, such materials need specific conditions to achieve dynamic adjustment of electromagnetic interference shielding effectiveness (EMI SE), urging the development of a simple and efficient strategy to regulate electromagnetic shielding performance without external stimulation.

Anisotropic materials with properties that vary according to direction are thus attracting increasing attention in smart EMI shielding. Among advanced carbon materials, graphene and CNTs are difficult to meet the above scenarios due to their difficulty in achieving anisotropy and complex preparation conditions,[11] respectively. CNFs with high aspect ratios and a

H. Feng, P. Chen, C. Tian, B.-W. Li
School of Materials Science and Engineering
Wuhan University of Technology
Wuhan 430070, P. R. China
E-mail: bwli@whut.edu.cn

X. Zhao, W. Qian, D. He
Hubei Engineering Research Center of Radio Frequency Microwave Technology and Application
Wuhan University of Technology
Wuhan 430070, P. R. China
E-mail: hedaping@whut.edu.cn

Z. Wang
State Key Laboratory of Advanced Technology for Materials Synthesis and Processing
Wuhan University of Technology
Wuhan 430070, P. R. China
E-mail: wangzhe0614@whut.edu.cn

The ORCID identification number(s) for the author(s) of this article can be found under https://doi.org/10.1002/smll.202408366

DOI: 10.1002/smll.202408366

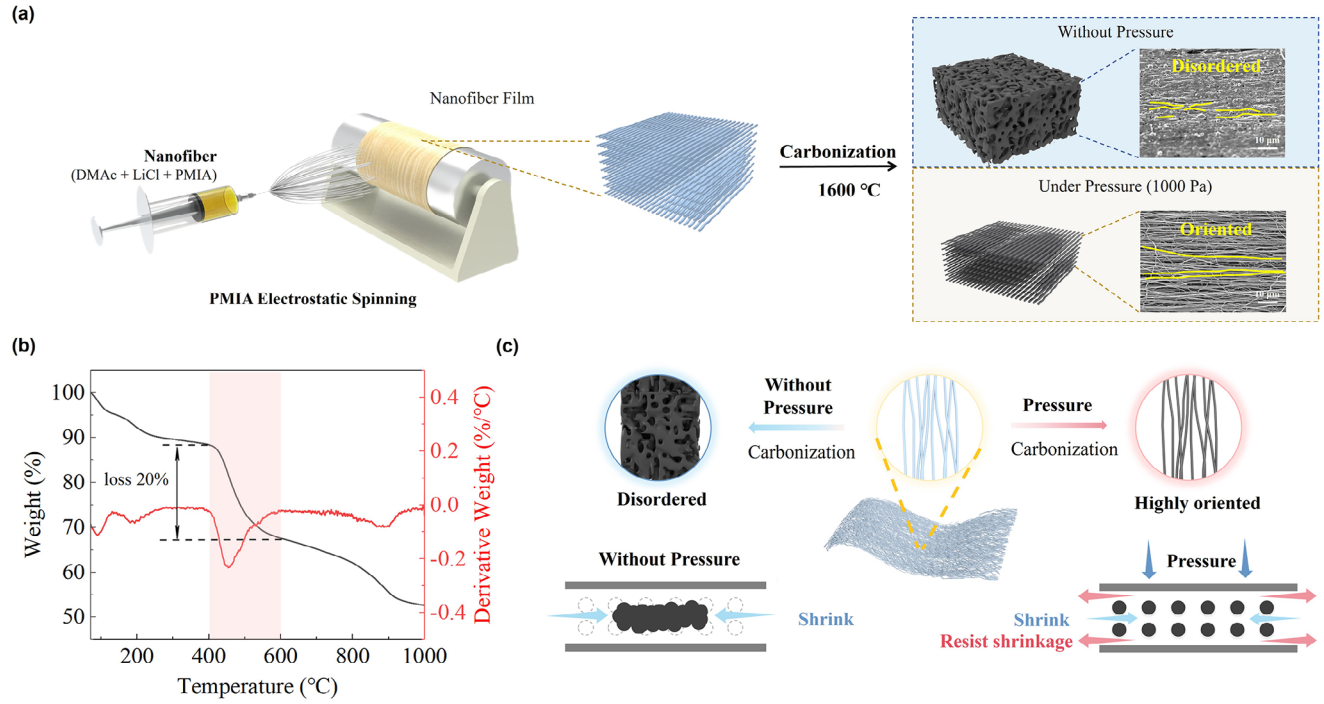

Figure 1. a) Schematic illustration of the preparation process. b) TG and DTG of CNFFs. c) Proposed mechanism for pressure-assisted alignment of CNFs during carbonization process.

simple synthesis process are very promising building blocks for such materials.[12] By the biaxial weaving of carbon fibers (CFs) and glass fibers, Hong et al. prepared anisotropic CF fabrics with a thickness of ≈1.03 mm to explore the effects of CF orientation on EMI SE.[13] Chen et al. used commercial cotton pads with oriented structure as a carbon source to prepare oriented CNF films via pyrolysis and achieved in-plane anisotropy in EMI SE,[14] and reduced the thickness to ≈0.3 mm. However, there still exist challenges, such as (millimeter-level) large thickness and the difficulty of delicate control of fiber orientation and anisotropy degree, which severely hamper their applications in portable devices and intelligent electromagnetic shielding field.

To tackle the challenges mentioned above, we proposed here a controllable synthetic route for carbon nanofiber films (CNFFs) with adjustable alignment via electrospinning and pressurized carbonization. The achieved aligned carbon nanofiber film (a-CNFF) features high electrical conductivity, small thickness, and low density, thus achieving an extremely high specific electromagnetic shielding effectiveness of 34 000 dB cm^2 g^{-1}. Impressively, the highly-oriented CNFs enable a direction-dependent electromagnetic shielding performance adjustable within the range of 23.0–35.6 dB in the X-band, allowing intelligent and dynamic electromagnetic shielding. Moreover, the a-CNFF also demonstrates efficient and surprising in-plane anisotropy in Joule heating, making it a very promising multifunctional material in the field of intelligent heating and intelligent shielding of linearly polarized electromagnetic waves in a specific direction.[15] The electromagnetic wave is linearly polarized in some applications, such as linearly polarized microwave radar systems, which play a crucial role in military target identification and weather surveillance.[16]

2. Results and Discussion

The a-CNFF with in-plane anisotropy was obtained via electrospinning and subsequent pressurized carbonization as illustrated in **Figure 1a**. First, the precursor solution was prepared by deprotonation of Poly (m-phenylene isophthalamide) (PMIA) with fiber diameters of 0.18 mm in the mixed solvent system of LiCl and *N*,*N*-Dimethylacetamide (DMAc) (Figure S1a, Supporting Information), resulting in a uniform dispersion of aramid nanofibers (ANFs) (Figure S1b, Supporting Information). The existence of LiCl deprotonates the hydroxyl protons in the amide NH of PMIA and the cations serving as proton donors lower the viscosity of ANFs dispersion. A rotating drum collector was used in the subsequent electrospinning process to achieve aligned ANFs. Rotating speed and electrospinning time were chosen to be 140 rev. min^{-1} and 4.5 h, respectively to obtain the aligned aramid nanofiber film (a-ANFF) with desired thickness and alignment. A digital photograph of the prepared a-ANFF is shown in Figure S1c (Supporting Information) and the uniaxial alignment of ANFs can be observed by the scanning electron microscope (SEM) image in Figure S1d (Supporting Information) featuring an average fiber diameter of 350 nm (Figure S2, Supporting Information).

To obtain the final CNFFs with enhanced conductivity, a two-step carbonization was carried out at 600 and 1600 °C (Figure S3, Supporting Information) yielding an obvious shrinkage of nanofibers from 350 to 250 nm (Figure S4, Supporting Information). These specific temperatures were chosen because the carbonization process is most violent within 400 to 600 °C as evidenced by the thermogravimetric analysis (Figure 1b) and the residual LiCl can be completely removed at 1600 °C. It is worth

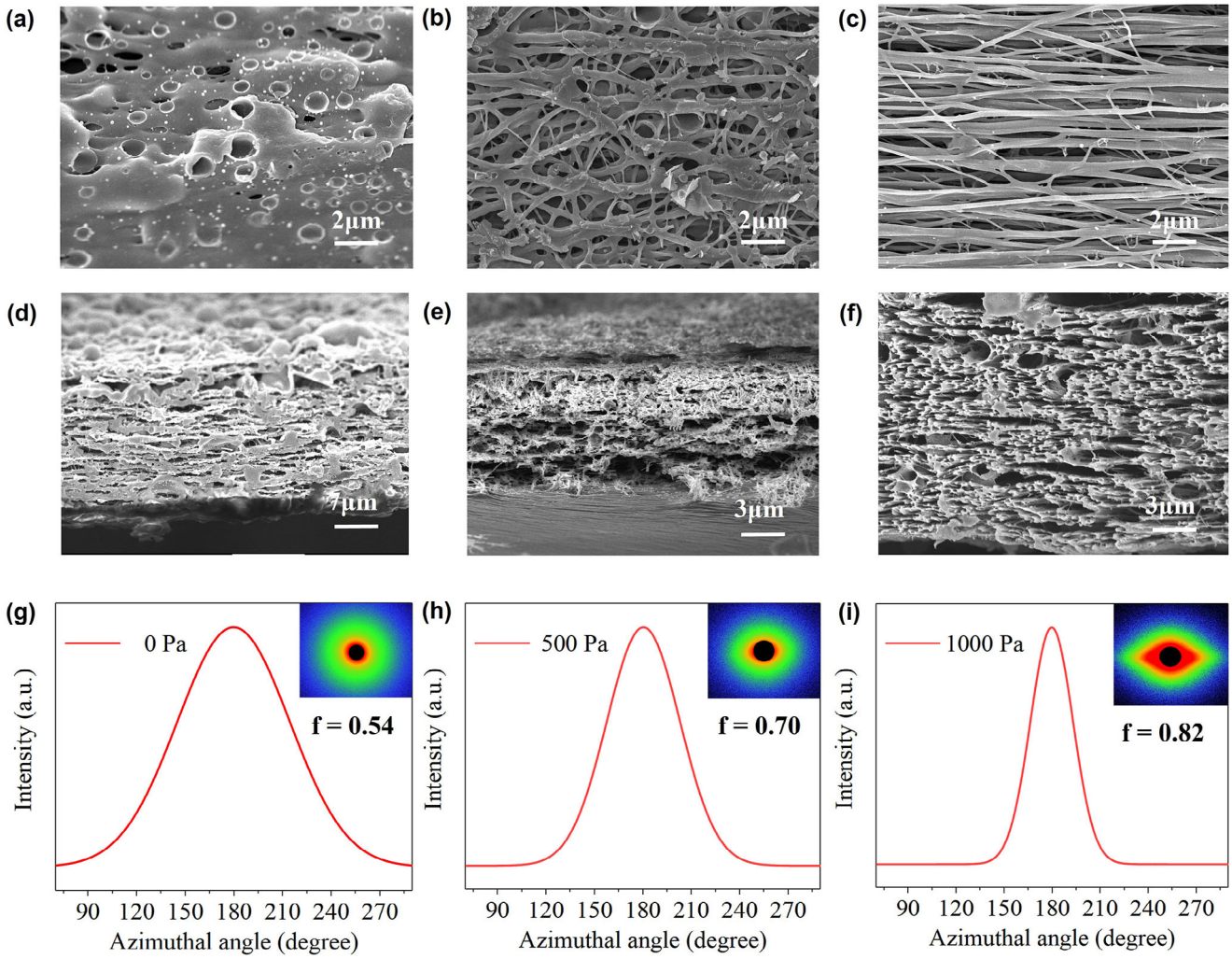

Figure 2. Top-view SEM images of a) n-CNFF, b) 2-CNFF and c) a-CNFF. Cross-sectional SEM images of d) n-CNFF, e) 2-CNFF and f) a-CNFF. 2D SAXS patterns with corresponding azimuthal-integrated intensity distribution curves of g) n-CNFF, h) 2-CNFF and i) a-CNFF.

noting that, by applying a pressure of 1000 Pa on the a-ANFF or not during the first carbonization process, two CNFFs with distinctively different configurations can be obtained as illustrated in Figure 1a. Specifically, when without applied pressure, the CNFs are distributed randomly with no orientation, and the film is denoted as n-CNFF. When with pressure treatment, the obtained CNFF is composed of uniaxially aligned CNFs and thus denoted as a-CNFF. A possible mechanism that results in the morphological difference is schematically illustrated in Figure 1c. If no applied pressure, C—C bonds are gradually formed between each fiber during the carbonization, linking the dispersed ANFs into a dense and large interconnected network with shrinkage in lateral dimension indicated by the blue arrows, and an increase in thickness. In the presence of applied pressure, lateral contraction of the a-ANFF during carbonization can be greatly suppressed due to the frictional forces between the film and the pressed graphite plates indicated by the red arrows, in turn, benefiting the maintenance of the highly aligned structure and thin thickness. When an even higher pressure of 1250 Pa was applied during the carbonization process, the film cracked. Excessive pressure may severely limit the contraction of the fiber, causing the membrane to crack along the fiber direction.

To verify the proposed mechanism of pressure-assisted anisotropy, more control samples were made with different applied pressures of 250, 500, and 750 Pa and denoted as 1, 2, and 3-CNFF, respectively. As evidenced by the top-view and cross-sectional SEM images in **Figure** 2a–d, the n-CNFF without pressure treatment features a layered and interconnected porous structure. The ANFFs tend to shrink and fuse during the carbonization process. If there is no pressure, the fibers will adhere to each other due to the overlap, and shrink to the inside of the film until the fibers fuse with each other, leaving only the holes left during the gas release process. When with pressure, improved orientation can be achieved as observed in 1, 2, and 3-CNFF (Figure 2b–e; Figure S5, Supporting Information), and a-CNFF (Figure 2c–f). More importantly, the degree of alignment of CNFs is dependent on the magnitude of the applied pressure. With increasing applied pressure from 0 to 1000 Pa, the alignment of CNFs increases as well, from a partially interconnected fiber network to orderly aligned carbon nanofibers.

The differences in alignment of the CNFFs were further confirmed by small-angle X-ray scattering (SAXS) analysis as illustrated in Figure 2h–j. From the azimuthal-integrated intensity profiles, we can see that the n-CNFF is in pure isotropic phase. With increasing applied pressure, the full width at half maximum (FWHM) decreases from 81.68° to 31.22°. Hence, the a-CNFF shows the highest order parameter of 0.82, higher than those for 1, 2, and 3-CNFFs (Figure S6, Supporting Information). These results demonstrate a systematic and controllable manipulation of CNF alignment. This proposed mechanism is also consistent with the better size retention observed in CNFFs with increasing applied pressures as shown in Figure S7 (Supporting Information). Specifically, starting with identical a-ANFFs of size 50 cm^2, the obtained n-CNFF and a-CNFF exhibited final size of 4.5 and 23.8 cm^2, respectively after carbonization at 1600 °C. As a result, the a-CNFF exhibits a much thinner thickness of ≈47 µm and a much lighter density of ≈0.17 g cm^{-3} compared to the n-CNFF (Figure S8, Supporting Information). In addition, according to Brunauer–Emmett–Teller (BET) surface area analysis, the specific surface area of n-CNFF is only 28.8556 m^2 g^{-1}, while that of a-CNFF is as high as 115.5261 m^2 g^{-1} (Table S1, Supporting Information).

Further physiochemical characterizations including Fourier transform infrared spectroscopy (FTIR), X-ray photoelectron spectroscopy (XPS), X-ray diffraction (XRD), and Raman spectroscopy were carried out to investigate the compositional and structural information of the obtained CNFFs. The decreased peak intensity at ≈3300 cm^{-1} (N—H stretching), 1540 cm^{-1} (C—N stretching), and 1306 cm^{-1} (Ph–N vibration) that are characteristic of ANF absorption after carbonization at 600 °C evidence the effective elimination of functional groups in ANF (Figure S9a,b, Supporting Information). After the second carbonization process at 1600 °C, the absorption peaks of C═O located at ≈1600 cm^{-1} disappeared, indicating a high degree of carbonization (Figure S9c, Supporting Information). This is further corroborated by the XPS survey spectra and high-resolution C 1s spectra in Figure S10 (Supporting Information). XRD patterns of the CNFFs reveal clear but broad peaks at $2\theta = 26°$, which can be indexed to the (002) diffraction planes of graphite, indicating the formation of layered graphite-like structure but with a low degree of graphitization and crystallization (Figure S11, Supporting Information). This is consistent with the Raman results in Figure S12 (Supporting Information). After carbonization at 600 °C, two characteristic peaks emerged at 1350 cm^{-1} (D-band) and 1580 cm^{-1} (G-band) (Figure S12a,b, Supporting Information), which are related to disordered carbon and sp^2 hybrid carbon, respectively. The D and G peaks represent the defects of the carbon lattice structure and the hybrid carbogen of the sp^2 vibration mode in the graphene plane. The calculated I_D/I_G ratios of CNFFs carbonized at 600 °C are ≈1 with broad peaks, indicating the existence of plentiful defects in the films. Further carbonization at 1600 °C decreased the peak widths, but the I_D/I_G ratios remained unchanged (Figure S12c, Supporting Information), which once again verifies the disordered and amorphous structure of CNFFs.

The two films with no anisotropy (n-CNFF) and with the most pronounced anisotropy (a-CNFF) were selected to investigate EMI shielding ability. Using a vector network analyzer, the total EMI SE (EMI SE_T) values were measured over the entire X-band (8.2–12.4 GHz). The a-CNFF and n-CNFF maintained EMI SE_T values above 23 and 43 dB for the entire X-band, respectively, corresponding to a shielding ratio of 99.5% and 99.995%. The n-CNFF shows higher EMI SE_T than the a-CNFF due to its larger thickness that allows longer travel distance for the EM wave, thus greatly increasing the loss of electromagnetic wave. To eliminate the effects of material density and thickness on EMI SE_T, EMI SSE/t defined as the SE divided by density and thickness is therefore a more reasonable parameter to evaluate the EMI shielding ability. Benefiting from its lightweight and micrometer thickness, the a-CNFF reveals an outstanding SSE/t value of 34 000 dB cm^2 g^{-1} with a thickness of ≈47 µm (**Figure 3a**), which outperforms most of the reported EMI shielding materials (Figure 3b; Table S2, Supporting Information). At the same time, the EMI shielding effectiveness per unit thickness (SE/t) of a-CNFF is calculated to be 5791 dB cm^{-1}. This seemingly mediocre value is reasonable considering the substantial inter-fiber spacing in the a-CNFF, which inevitably leads to lower SE/t compared to dense materials like Al foil. However, the areal density of a-CNFF is only 1/3 of Al foil, fulfilling the requirements for miniaturization and reduced weight in EMI shielding applications.

To gain more insight into the outstanding performance of EMI shielding, the electrical conductivities of the CNFFs were measured with a four-point probe system, giving ultrahigh conductivity of 1572 S m^{-1} for a-CNFF and 4675 S m^{-1} for n-CNFF, consistent with the EMI SE results. Compared with the nanofiber network structure of a-CNFF, n-CNFF has a higher density, providing a larger space for the migration of free electrons within the film, resulting in superior electrical conductivity and better EMI SE. It was expected that the orientation of CNFs would lead to anisotropic electrical properties, thus, the electrical conductivities of the a-CNFF were measured both parallel (denoted as 'X') and transverse (denoted as 'Y') to the axial direction of the fibers as illustrated in the inset of Figure 3c. The conductivity of CNFFs in the X direction and Y direction were measured by volume resistance measurement. In contrast to the direction-independent conductivity of n-CNFF, the a-CNFF exhibits obvious anisotropy in conductivity with an X/Y ratio of ≈4.58 (Figure 3c; Table S3, Supporting Information). Inspired by this, direction-dependent EMI shielding performance was evaluated by rotating the sample while fixing the polarization direction of the incident wave.

As illustrated in Figure 3d, the rotation angle is defined as 0° when the alignment direction of carbon nanofibers is transverse to the polarization direction of the incident electric field. The EMI SE_T values were recorded in the X-band (Figure S13, Supporting Information) and the average SE_A, SE_R, and SE_T values were obtained (Table S4, Supporting Information) when rotating the a-CNFF from 0° to 180° with a step size of 30°. Obvious anisotropy in EMI SE can be observed when plotting the average EMI SE_A, SE_R, and SE_T values in the X-band as a function of rotation angle (Figure 3e). Specifically, the EMI SE_T increases as the rotation angle increases from 0° to 90° and then decreases from 90° to 180°, showing an expected axial symmetric variation ≈90°. This monotonous increase/decrease in SE_T values allows a controllable and dynamic EMI shielding performance with a modulating range of 23.0–35.6 dB. Meanwhile, to explore the EMI SE of a-CNFF in 1–12.4 GHz, it was investigated by coaxial method (Figure S14, Supporting Information). The EMI SE

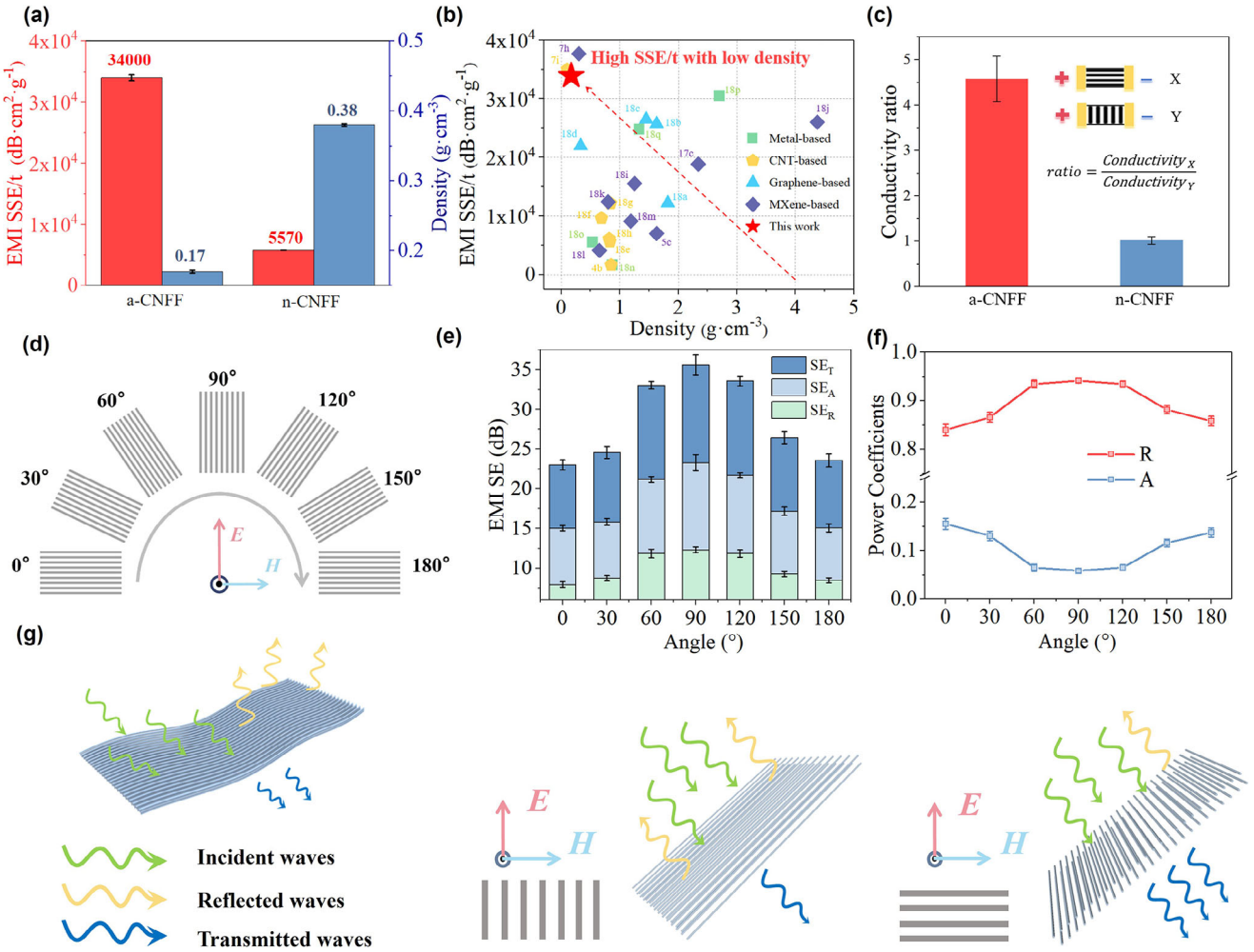

Figure 3. a) SSE/t and density of a-CNFF and n-CNFF. b) Comparison of SSE/t and density between the a-CNFF and other reported films.[4b,5c,7h–l,17c,18] c) Conductivity ratios along X and Y of a-CNFF and n-CNFF. d) Schematic diagram of polarization-dependent electromagnetic shielding test. e) EMI SE of a-CNFF at various angles (0°–180°). f) Coefficients of reflection and absorption of a-CNFF at various angles (0°–180°). g) Proposed mechanism of polarization-dependent EMI SE in a-CNFF.

obtained via the coaxial and waveguide methods are not entirely consistent, primarily due to differences in the polarization modes of the electromagnetic waves in the two methods. In the waveguide method, the electromagnetic wave is linearly polarized, resulting in significant variations in EMI SE at different rotation angles (e.g., 0° and 90°, corresponding to the alignment of carbon nanofibers being parallel and perpendicular to the polarization direction of the incident electric field, respectively). In contrast, the electromagnetic wave in the coaxial method is not linearly polarized, and the EMI SE remains consistent across different rotation angles (e.g., 0° and 90°, defined as the initial and rotated sample placements, respectively) in Figure S15, (Supporting Information). To gain further insight into the dynamic interaction between linearly polarized EM waves and the alignment of carbon nanofibers, the reflection and absorption ratios were calculated. As depicted in Figure 3f, the reflection coefficients vary with rotation angle following the same trend as EMI SE_T with a minimum of 0.839 at 0°/180° and a maximum of 0.941 at 90°. Meanwhile, the absorption coefficients exhibit an opposite trend with a minimum of 0.058 at 90° and a maximum of 0.155 at 0°/180°. These results illustrate a dominating role of reflection and reveal the possible mechanism for the dynamic EMI shielding effectiveness of a-CNFF as depicted in Figure 3g and Figure S16 (Supporting Information). When the rotation angle is set to 90°, the incident electric field aligns parallel to the fiber arrangement. The continuous conductive path within the a-CNFF facilitates the maximization of the electric conductivity. A high impedance mismatch can be realized at the interface, consequently leading to a more efficient attenuation of the electromagnetic waves. As a result, higher SE_R is generated, multiple reflections of electromagnetic waves in the membrane are enhanced, and SE_A is improved. When the rotation angle is set to 0° or 180°, the incident electric field is perpendicular to the fiber arrangement. Due to the discontinuous conductive path, the minimized impedance mismatch allows more incident EM waves to penetrate the a-CNFF, and only a relatively low EMI SE is displayed. In addition, the electromagnetic shielding effectiveness of n-CNFF,1-CNFF,2-CNFF, and 3-CNFF in the X-band was also measured (Figure S17 and

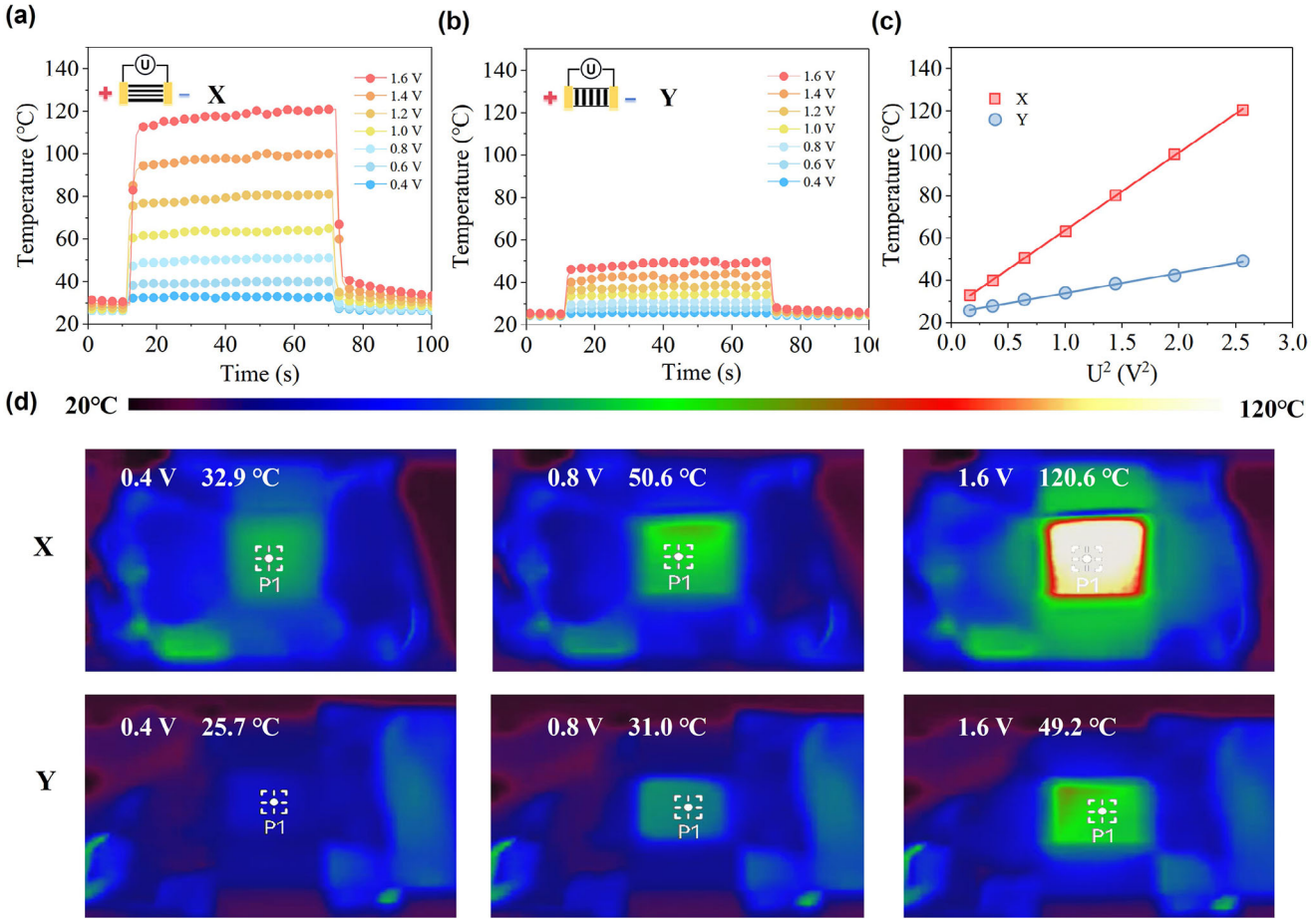

Figure 4. Time-dependent temperature curves of a-CNFF under different applied voltages along a) X direction and b) Y direction. c) Linear fitting of saturation temperature to the square of the voltage. d) Infrared thermal images of the film at various voltages with different test configurations.

Tables S5–S8, Supporting Information). With the increase in pressure, the anisotropy of electromagnetic shielding gradually became obvious.

Carbon-based materials have the potential to convert electrical energy into heat due to their much lighter density and higher current-carrying capacity compared to metals. Given the merits of high and direction-dependent conductivity, bio-compatibility, and flame retardancy, the proposed a-CNFF can serve as a compelling candidate material for smart electric heaters. The Joule heating performance of a-CNFF (12 × 10 mm^2) was tested at various voltages by connecting it to a DC power supply and adjusting the voltages to 0.4, 0.6, 0.8, 1.0, 1.2, 1.4, and 1.6 V (Table S9, Supporting Information). Intriguingly, by applying the voltage along different directions of the film as depicted in the insets of **Figure** 4a,b, the film showed distinctively different heating performances. Specifically, the voltage is applied either parallel (X) or transverse (Y) to the alignment direction of the carbon nanofibers while keeping the heating area the same. When being applied with the same voltage, the parallel case showed a much higher saturation temperature than the transverse case. For instance, at 1.6 V, the surface temperature can reach 120.6 °C for the parallel configuration but can only reach 49.2 °C for the transverse case (Figure 4a,b). With both configurations, the steady-state saturation temperature T_s can be reached within 3 s, revealing a rapid and voltage-sensitive thermal response. By fitting the steady-state temperature on the surface of the film to the square of the voltage (Figure 4c), a perfect linear relationship can be obtained, which proves the consistency of Joule's law. IR images were also recorded to vividly show the evolution of surface temperature upon increasing applied voltage for the two cases (Figure 4d; Figures S18, S19, Supporting Information). The much more efficient electro-thermal conversion in the parallel case can be attributed to the higher conductivity along the axial direction of the a-CNFF. Overall, the a-CNFF exhibits unique electro-thermal conversion effectiveness and fast thermal response, making it promising in the applications of wearable electric heaters that work at low voltage under 12 V for safety reasons. Notably, the Joule heating effectiveness of other reported electrothermal materials[7g,17] was also summarized and compared with that of a-CNFF (Table S10, Supporting Information), where a-CNFF demonstrated advantages over most prior works. The a-CNFF exhibits anisotropic characteristics in terms of Joule heating efficiency and can achieve higher surface temperature when lower voltage and power density are applied, making it promising in the field of intelligent heating.

3. Conclusion

In summary, anisotropic carbon nanofiber films were prepared by electrospinning and subsequent pressure-assisted carbonization. The electrical conductivity of the a-CNFF is notably anisotropic, with values of 2134 S m^{-1} in the X direction and 466 S m^{-1} in the Y direction, yielding a conductivity ratio of X to Y as high as 4.58. Concurrently, the a-CNFF has a low density of 0.17 g cm^3 and a porosity reaching 76%, complemented by a specific surface area of 115.5261 m^2 g^{-1}. The highly aligned carbon nanofibers in the film with micrometer thickness enable an efficient and smart adjustment of EMI SE from 23.0 to 35.6 dB for linearly polarized electromagnetic waves within the entire X-band. The a-CNFF exhibits a superior SSE/t of 33 400 dB cm^2 g^{-1}, along with an EMI SE per unit thickness of 5791 dB cm^{-1}. Also, given the lightweight and high current-carrying capacity, the a-CNFF demonstrates superb and tailorable Joule heating performances with direction-dependent steady temperature controllable within the range of 49.2–120.6 °C under the same applied voltage of 1.6 V. It is also worth noting with the proposed fabrication method, the degree of anisotropy can be easily controlled by applying different pressures during carbonization, rendering the films with more possible applications in electronic communications, military, aerospace, microelectronics, and smart wearable electronics.

4. Experimental Section

Materials: Poly (m-phenylene isophthalamide) (PMIA) was purchased from Dongguan Haiyuan Textile Co., Ltd. Lithium chloride (LiCl, AR, ≥99.995%) and *N*,*N*-Dimethylacetamide (DMAc, AR) were purchased from Aladdin Reagent Co., Ltd. All chemicals were used as received without further purification.

Fabrication of CNFFs: LiCl (0.5 g) was first added into 25 mL DMAc followed by constant magnetic stirring for 30 min to obtain a uniform LiCl/DMAc solution. Then 2.5 g of PMIA was added into the obtained solution and dissolved by constant stirring at 80 °C for 12 h to prepare the uniform dispersion of ANFs with a weight fraction of 10 wt.%. The obtained ANFs dispersion (2 mL) was loaded into a syringe for electrospinning (ET-1, Beijing Yongkang Leye Technology Development Co., Ltd.). Specifically, the extrusion rate, output voltage, relative humidity, and temperature were set to be 0.02 mm min^{-1}, 18 kV, 50%, and 25 °C, respectively. By using the rotating drum collector with a rotating speed of 140 rev min^{-1}, a-ANFF can be obtained. The prepared a-ANFF film sample was sandwiched in two graphite plates with a length of 100 mm and a width of 50 mm, and the film was subjected to different pressures uniformly by adding weights (Figure S20, Supporting Information). The carbonization process was carried out in a high-temperature tube furnace (GSL-1700X, Hefei Kejing Material Technology Co., LTD.). At the same time, the prepared a-ANFF was sandwiched in two graphite sheets, and the film was subjected to different pressures uniformly by adding heavy objects. Two-step carbonization process was then carried out in N_2 atmosphere at 600 °C for 1 h and 1600 °C for 30 min with a ramp rate of 1 and 4 °C min^{-1}, respectively to obtain CNFFs. In the first carbonization process, five different samples were obtained under different pressures of 0, 250, 500, 750, and 1000 Pa, namely n-CNFF, 1-CNFF, 2-CNFF, 3-CNFF, and a-CNFF.

EMI Shielding and Joule Heating Performance: Electromagnetic interference shielding measurements of carbon nanofiber films were carried out in a rectangular waveguide using a vector network analyzer (VNA, Keysight N5225A) in X-band frequency range (8.2–12.4 GHz). The samples were cut into a rectangular shape, slightly larger in dimension (25 mm × 25 mm) as compared to the opening of the sample holder (10.2 mm × 22.9 mm). While mounting the film onto the sample holder, extra care was taken to avoid any leakage paths from the edges. The sample holder was tightly fixed with screws. Based on the measured results, the coefficients of reflection (R), transmission (T), and absorption (A) can be determined using the following formula.

$$R = |S_{11}|^2 \tag{1}$$

$$T = |S_{21}|^2 \tag{2}$$

$$A = 1 - R - T \tag{3}$$

The reflection loss (SE_R), absorption loss (SE_A), and total shielding effectiveness (SE_T) can then be determined as:

$$SE_R = -10 \log (1 - R) \tag{4}$$

$$SE_A = -10 \log \left(\frac{T}{1 - R} \right) \tag{5}$$

$$SE_T = SE_R + SE_A \tag{6}$$

The absolute effectiveness of EMI shielding (SSE/t) taking account of both the density and thickness of a material is defined as below:

$$\frac{SSE}{t} = \frac{SE}{density \times thickness} \tag{7}$$

For Joule heating tests, the applied voltage was provided by a direct current (DC) power supply (Rigol, DP832), and the surface temperature distribution was recorded using an infrared (IR) camera (HM-TPK20-3AQF/W).

Supporting Information

Supporting Information is available from the Wiley Online Library or from the author.

Acknowledgements

The authors acknowledge financial support from the National Natural Science Foundation of China (22279097), the Key R&D Program of Hubei Province (2023BAB103), the Foundation of National Key Laboratory of Microwave Imaging Technology, and the Natural Science Foundation of Hubei Province (JCZRQN202500109).

Conflict of Interest

The authors declare no conflict of interest.

Data Availability Statement

The data that support the findings of this study are available from the corresponding author upon reasonable request.

Keywords

alignment control, carbon nanofibers, electromagnetic interference shielding, electrospinning, joule heating

Received: September 17, 2024
Revised: February 14, 2025
Published online: March 6, 2025

[1] a) T. Nan, H. Lin, Y. Gao, A. Matyushov, G. Yu, H. Chen, N. Sun, S. Wei, Z. Wang, M. Li, X. Wang, A. Belkessam, R. Guo, B. Chen, J. Zhou, Z. Qian, Y. Hui, M. Rinaldi, M. E. McConney, B. M. Howe, Z. Q. Hu, J. G. Jones, G. J. Brown, N. X. Sun, *Nat. Commun.* **2017**, *8*, 8; b) J. Cheng, H. Zhang, M. Ning, H. Raza, D. Zhang, G. Zheng, Q. Zheng, R. Che, *Adv. Funct. Mater.* **2022**, *32*, 12.

[2] a) Z. Yu, T. Dai, S. Yuan, H. Zou, P. Liu, *ACS Appl. Mater. Interfaces* **2020**, *12*, 30990; b) S. Li, X. Tang, Y. Zhang, Q. Lan, Z. Hu, L. Li, N. Zhang, P. Ma, W. Dong, W. Tjiu, Z. Wang, T. Liu, *ACS Appl. Mater. Interfaces* **2022**, *14*, 8297; c) Z. Ma, S. Kang, J. Ma, L. Shao, Y. Zhang, C. Liu, A. Wei, X. Xiang, L. Wei, J. Gu, *ACS Nano* **2020**, *14*, 8368.

[3] a) S. K. Srivastava, K. Manna, *J. Mater. Chem. A* **2022**, *10*, 7431; b) J. Cheng, C. Li, Y. Xiong, H. Zhang, H. Raza, S. Ullah, J. Wu, G. Zheng, Q. Cao, D. Zhang, Q. Zheng, R. Che, *Nano-Micro Lett.* **2022**, *14*, 31.

[4] a) F. Shahzad, M. Alhabeb, C. B. Hatter, B. Anasori, S. M. Hong, C. M. Koo, Y. Gogotsi, *Science* **2016**, *353*, 1137; b) H. Guo, Y. Li, Y. Ji, Y. Chen, K. Liu, B. Shen, S. He, G. Duan, J. Han, S. Jiang, *Compos. Commun.* **2021**, *27*, 100879.

[5] a) Z. Zeng, F. Jiang, Y. Yue, D. Han, L. Lin, S. Zhao, Y.-B. Zhao, Z. Pan, C. Li, G. Nyström, J. Wang, *Adv. Mater.* **2020**, *32*, 7; b) Z. Xiang, Y. Shi, X. Zhu, L. Cai, W. Lu, *Nano-Micro Lett.* **2021**, *13*, 21; c) B. Zhou, Z. Zhang, Y. Li, G. Han, Y. Feng, B. Wang, D. Zhang, J. Ma, C. Liu, *ACS Appl. Mater. Interfaces* **2020**, *12*, 4895; d) L. Shen, Y. Li, W. Zhao, K. Wang, X. Ci, Y. Wu, G. Liu, C. Liu, Z. Fang, *J. Mater. Sci. Technol.* **2020**, *44*, 121.

[6] a) Y. Chen, L. Pang, Y. Li, H. Luo, G. Duan, C. Mei, W. Xu, W. Zhou, K. Liu, S. Jiang, *Compos. Part A-Appl. Sci.* **2020**, *135*, 9; b) Z. Wang, B. Mao, M. Zhao, D. G. Calatayud, W. Qian, P. Li, Z. Hu, H. Fu, X. Zhao, S. Yan, Z. Kou, D. He, *ACS Nano* **2022**, *16*, 3934; c) Z. Wang, P. Li, R. Song, W. Qian, H. Zhou, Q. Wang, Y. Wang, X. Zeng, L. Ren, S. Yan, S. Mu, D. He, *Sci. Bull.* **2020**, *65*, 1363; d) Z. Wang, B. Mao, Q. Wang, J. Yu, J. Dai, R. Song, Z. Pu, D. He, Z. Wu, S. Mu, *Small* **2018**, *14*, 8; e) M. Li, B. Yin, C. Gao, J. Guo, C. Zhao, C. Jia, X. Guo, *Exploration* **2023**, *3*, 20210233.

[7] a) T. Yun, H. Kim, A. Iqbal, Y. S. Cho, G. S. Lee, M. K. Kim, S. J. Kim, D. Kim, Y. Gogotsi, S. O. Kim, C. M. Koo, *Adv. Mater.* **2020**, *32*, 1906769; b) D.-C. Wang, Y. Lei, W. Jiao, Y.-F. Liu, C.-H. Mu, X. Jian, *Rare Met.* **2021**, *40*, 3; c) H. Liang, H. Xing, M. Qin, H. Wu, *Compos. Part A-appl. S.* **2020**, *135*, 105959; d) Y. Zhang, Y. Shen, M. Dang, F. Zhang, X. Du, *Ceram. Int.* **2021**, *47*, 9178; e) A. Sheng, Y. Yang, D.-X. Yan, Dai, H. D, G. Zhao, Y. Liu, Z.-M. Li, *Carbon* **2020**, *167*, 530; f) H. Xu, X. Yin, M. Li, X. Li, X. Li, X. Dang, L. Zhang, L. Cheng, *ACS Appl. Mater. Interfaces* **2019**, *11*, 22628; g) W. Qian, H. Fu, Y. Sun, Z. Wang, H. Wu, Z. Kou, B.-W. Li, D. He, C.-W. Nan, *Adv. Mater.* **2022**, *34*, 8; h) X.-A. Ye, S.-Y. Zhang, D.-Q. Zhao, L. Ding, K. Fang, X. Zhou, G.-G. Wang, *Compos. Part A-Appl. Sci.* **2024**, *176*, 107866; i) S. J. P. Gamage, K. Yang, R. Braveenth, K. Raagulan, H. S. Kim, Y. S. Lee, C. M. Yang, J. J. Moon, K. Y. Chai, *Materials* **2017**, *10*, 11; j) T. T. L. Nguyen, S. J. Cho, J. Ko, D. C. T. Nguyen, M. W. Kim, N. D. Kim, D. S. Lee, Y. Joo, *Carbon* **2024**, *230*, 9; k) H. Zhang, X. Gong, X. Dai, Z. Yong, S. Ramakrishna, *iScience* **2024**, *27*, 12; l) X. Shen, J. K. Kim, *Matter* **2019**, *1*, 796.

[8] a) S.-S. Yao, F.-L. Jin, K. Y. Rhee, D. Hui, S.-J. Park, *Compos. Part B-Eng.* **2018**, *142*, 241; b) R. Kumar, S. Sahoo, E. Joanni, R. K. Singh, W. K. Tan, K. K. Kar, A. Matsuda, *Carbon* **2021**, *177*, 304; c) D. D. L. Chung, *Carbon* **2001**, *39*, 279.

[9] a) X. Hou, X.-R. Feng, K. Jiang, Y.-C. Zheng, J.-T. Liu, M. Wang, *J. Mater. Sci. Technol.* **2024**, *186*, 256; b) C. Liang, H. Qiu, Y. Zhang, Y. Liu, J. Gu, *Sci. Bull* **2023**, *68*, 1938; c) X. Chen, Y. Gu, J. Liang, M. Bai, S. Wang, M. Li, Z. Zhang, *Compos. Part A-Appl. Sci.* **2020**, *139*, 106099.

[10] a) B. A. Al-Asbahi, S. M. H. Qaid, A. A. A. Ahmed, A. G. El-Shamy, *Mater. Chem. Phys.* **2023**, *293*, 126922; b) P. Kumar, U. N. Maiti, A. Sikdar, T. K. Das, A. Kumar, V. Sudarsan, *Polym. Rev.* **2019**, *59*, 687; c) Z. Li, Y. Sun, B. Zhou, Y. Feng, C. Liu, C. Shen, *Mater. Today Phys.* **2023**, *32*, 9; d) Y. Zhang, J. Gu, *Nano-Micro Lett.* **2022**, *14*, 9; e) M. Han, D. Zhang, C. E. Shuck, B. McBride, T. Zhang, R. Wang, K. Shevchuk, Y. Gogotsi, *Nat. Nanotechnol.* **2023**, *18*, 9.

[11] a) B. Li, Y. Yang, N. Wu, S. Zhao, H. Jin, G. Wang, X. Li, W. Liu, J. Liu, Z. Zeng, *ACS Nano* **2022**, *16*, 19293; b) Y.-J. Wan, X.-Y. Wang, X.-M. Li, S.-Y. Liao, Z.-Q. Lin, Y.-G. Hu, T. Zhao, X.-L. Zeng, C.-H. Li, S.-H. Yu, P.-L. Zhu, R. Sun, C.-P. Wong, *ACS Nano* **2020**, *14*, 14134.

[12] a) B. Wen, X. Wang, Y. Zhang, *Compos. Sci. Technol.* **2019**, *169*, 127; b) X. Hong, D. D. L. Chung, *Carbon* **2017**, *111*, 529; c) J. Li, E. Masghouni, M. Granger, G. Sudre, P. Alcouffe, D. Muller, V. Nguyen, B. Bayard, A. Serghei, B. Sauviac, A. Maazouz, K. Lamnawar, *Macromol. Mater. Eng.* **2024**, *309*, 31; d) X. Jiang, H. Yu, H. Lu, Y. Si, Y. Dong, Y. Zhu, C. Qian, Y. Fu, *ACS Appl. Polym. Mater.* **2023**, *5*, 4400.

[13] X. Hong, L. Zhong, J. Wan, Y. Li, F. Guan, G. Wang, C. Zhu, Z. Jin, *Text. Res. J.* **2022**, *92*, 269.

[14] J. Chen, D. Yi, X. Jia, G. Wang, Z. Sun, L. Zhang, Y. Liu, B. Shen, W. Zheng, *J. Mater. Sci. Technol.* **2022**, *103*, 98.

[15] a) Z. Deng, L. Li, P. Tang, C. Jiao, Z.-Z. Yu, C. M. Koo, H.-B. Zhang, *ACS Nano* **2022**, *16*, 16976; b) Y. Wei, C. Hu, Z. Dai, Y. Zhang, W. Zhang, X. Lin, *Compos. Part A-Appl. Sci.* **2023**, *168*, 107476.

[16] X. Cao, Y. Qi, G. Ni, *J. Hydrol.* **2023**, *617*, 12.

[17] a) J.-J. Liu, C.-Y. He, B.-H. Liu, Z.-Q. Wang, S.-J. Zhao, Z.-W. Lu, Y.-Z. Zhang, Z.-Q. Tang, X.-H. Gao, X. Aday, *Chem. Eng. J.* **2024**, *489*, 12; b) H. Ba, L. Truong-Phuoc, T. Romero, C. Sutter, J. M. Nhut, G. Schlatter, G. Giambastiani, C. Pham-Huu, *Carbon* **2021**, *182*, 655; c) C. Liu, Y. Ma, Y. Xie, J. Zou, H. Wu, S. Peng, W. Qian, D. He, X. Zhang, B.-W. Li, C.-W. Nan, *ACS Appl. Mater. Interfaces* **2023**, *15*, 4516; d) Y. Guo, H. Zhao, C. Zhang, G. Zhao, *Chem. Eng. J.* **2024**, *497*, 14; e) Q. Chen, X. Shen, Z. Zhang, Q. Xu, *Prog. Org. Coat.* **2024**, *191*, 16; f) L. Wang, K. Yin, Q. Deng, Q. Huang, C. J. Arnusch, *Carbon* **2024**, *219*, 118824; g) Y. Sun, D. Li, J. U. Kim, B. Li, S.-H. Cho, T.-I. Kim, J.-D. Nam, L. J. Ci, J. Suhr, *Carbon* **2021**, *171*, 758; h) H. Im, E. Y. Jang, A. Choi, W. J. Kim, T. J. Kang, Y. W. Park, Y. H. Kim, *ACS Appl. Mater. Interfaces* **2012**, *4*, 2338; i) E.-C. Cho, C.-W. Chang-Jian, J.-H. Huang, R. T. Wu, C.-Z. Lu, K.-C. Lee, H. C. Weng, S. C. Hsu, *J. Taiwan Inst. Chem. Eng.* **2021**, *119*, 224; j) A. Ahmed, M. A. Jalil, M. M. Hossain, M. Moniruzzaman, B. Adak, M. T. Islam, M. S. Parvez, S. Mukhopadhyay, *J. Mater. Chem. C* **2020**, *8*, 16204; k) Q. Zhang, Y. Yu, K. Yang, B. Zhang, K. Zhao, G. Xiong, X. Zhang, *Carbon* **2017**, *124*, 296; l) J. Huang, Z. Peng, B. Zhang, Y. Yao, S. Chen, *ACS Appl. Mater. Interfaces* **2024**, *16*, 44210; m) Z. Wang, W. Yu, C. Gao, Z. Zhu, J. Zhang, *npj Flex. Electron.* **2024**, *8*, 10; n) F. Hu, M. Kui, J. Zeng, P. Li, T. Wang, J. Li, B. Wang, C. Wu, K. Chen, *ACS Nano* **2024**, *18*, 25852; o) Z. Lei, S. Duan, X. Wu, C. Gao, L. Wang, X. Min, Z. Huang, M. Fang, R. Luo, B. Luo, *J. Mater. Res. Technol.* **2023**, *23*, 1013; p) C. Li, Y.-T. Xu, B. Zhao, L. Jiang, S.-G. Chen, J.-B. Xu, X.-Z. Fu, R. Sun, C.-P. Wong, *J. Mater. Sci.* **2016**, *51*, 1043; q) H. Jiang, H. Wang, G. Liu, Z. Su, J. Wu, J. Liu, X. Zhang, Y. Chen, W. Zhou, *J. Alloy. Compd.* **2017**, *699*, 1049; r) Y. Liao, Y. Tian, X. Ma, M. Zhao, J. Qian, X. Wang, *ACS Appl. Mater. Interfaces* **2020**, *12*, 48077; s) Y. Liu, X. Ma, H. Zhang, J. Sun, J. Qian, X. Wang, *ACS Appl. Electron. Mater.* **2022**, *4*, 814; t) W. Chen, S. Yang, H. Wang, K. Yang, X. Wu, F. Gao, B. Zheng, K. Qian, W. Yao, T. Zhang, B. Zhong, X. Huang, *Chem. Eng. J.* **2022**, *431*, 9.

[18] a) M. C. Vu, P. J. Park, S. R. Bae, S. Y. Kim, Y. M. Kang, W. K. Choi, M. A. Islam, J. C. Won, M. Park, S. R. Kim, *J. Mater. Chem. A* **2021**, *9*, 8527; b) E. Zhou, J. Xi, Y. Liu, Z. Xu, Y. Guo, L. Peng, W. Gao, J. Ying, Z. Chen, C. Gao, *Nanoscale* **2017**, *9*, 18613; c) E. Zhou, J. Xi, Y. Guo, Y. Liu, Z. Xu, L. Peng, W. Gao, J. Ying, Z. Chen, C. Gao, *Carbon* **2018**, *133*, 316; d) D. W. Lee, H. Kim, J. S. Hyeon, J. H. Moon, B.-J. Kim, J.-H. Jeong, J. Choi, R. H. Baughman, G. M. Spinks, G. G. Wallace, S. J. Kim, *ACS Appl. Mater. Interfaces* **2020**, *12*, 46883; e) S. Lu, J. Shao, K. Ma, D. Chen, X. Wang, L. Zhang, Q. Meng, J. Ma, *Carbon* **2018**, *136*, 387; f) M. Fan, X. Xia, S. Li, R. Zhang, L. Wu, M. Qu, P. Tang, Y. Bin, *Chem. Eng. J.* **2022**, *441*, 136103; g) D. Zhang, W. Song, L. Lv, C. Gao, F. Gao, H. Guo, R. Diao, W. Dai, J. Niu, X. Chen, J. Wei, M. Terrones,

Y. Wang, *Carbon* **2023**, *214*, 118315; h) F. Jia, Z. Lu, Y. Liu, J. Li, F. Xie, J. Dong, *ACS Appl. Mater. Interfaces* **2022**, *4*, 6342; i) F. Xie, F. Jia, L. Zhuo, Z. Lu, L. Si, J. Huang, M. Zhang, Q. Ma, *Nanoscale* **2019**, *11*, 23382; j) B. Wang, W. Zhang, J. Sun, C. Lai, S. Ge, H. Guo, Y. Liu, D. Zhang, *J. Mater. Chem. A* **2023**, *11*, 8656; k) Y. Wang, T. Li, B. Shiu, X. Zhang, H. Peng, C. Lou, J. Lin, *Appl. Surf. Sci.* **2022**, *574*, 151552; l) W. Liang, J. Wu, S. Zhang, P. Zhao, Y. Cong, Y. Guo, G. Wang, *Nano Res.* **2024**, *17*, 2070; m) F. Jia, J. Dong, X. Dai, Y. Liu, H. Wang, Z. Lu, *Chem. Eng. J.* **2023**, *452*, 139395; n) Y. Pan, M. Dai, Q. Guo, D. Yin, S. Hu, N. Hu, X. Zheng, J. T. Huang, *Chem. Eng. J.* **2023**, *471*, 144301; o) T.-W. Lee, S.-E. Lee, Y. G. Jeong, *ACS Appl. Mater. Interfaces* **2016**, *8*, 13123; p) J. Liu, H.-B. Zhang, R. Sun, Y. Liu, Z. Liu, A. Zhou, Z.-Z. Yu, *Adv. Mater.* **2017**, *29*, 1702367; q) C. Wang, Y. Gong, B. V. Cunning, S. Lee, Q. Le, S. R. Joshi, O. Buyukcakir, H. Y. Zhang, W. K. Seong, M. Huang, M. Wang, J. Lee, G.-H. Kim, R. S. Ruoff, *Sci. Adv.* **2021**, *7*, eabe3767.